Photocatalytic Performance of Alkaline Activated Graphitic Carbon Nitride Under Blue LED Light

Yong OUYANG [1], Jianquan XU [1], Aiyu YANG [1], Caixia ZHONG [1], Wenjing HU [1], Shenglei FENG [1, 2] [∗], Youpeng HOU [1]

[1] *School of Environment and Energy, Jiangxi Modern Polytechnical College, Nanchang 330098, China*
[2] *College of Civil Engineering, Hebei University of Engineering, Handan 056038, China*

Graphitic carbon nitride (g-C$_3$N$_4$) is a metal-free photocatalyst with visible light response. However, the disadvantages limit its application in a wider range, such as its small specific surface areas, fewer active sites, narrow visible light absorption range and high photogenic carrier recombination. In this paper, NaOH was used as an activator for alkaline activation of g-C$_3$N$_4$. The phase composition, micromorphology, surface chemical state and optical properties of g-C$_3$N$_4$ after activation were tested. The photocatalytic performance of g-C$_3$N$_4$ over organic dyes was also tested. The results showed that Na$^+$ entered the interlayers of g-C$_3$N$_4$, expanding the spaces between layers. The specific surface area and pore volume of powder were increased. The active sites were increased. The band gap was decreased, and the photogenic carrier recombination was reduced. Alkaline activated g-C$_3$N$_4$ had better adsorption and degradation performance over rhodamine B and methyl orange than inactivated g-C$_3$N$_4$. Therefore, the alkaline activated g-C$_3$N$_4$ promotes its further application in the field of wastewater treatment. This work sheds light on the material modification through a simple method with the aim to efficiently use solar energy.

Keywords: g-C$_3$N$_4$, alkaline activation, photocatalysis, organic dyes, blue LED.

1. INTRODUCTION

With the development of industrialization, the discharge of industrial wastewater from industries such as printing and dyeing, pesticides and chemicals is increasing seriously. In particular, azo dyes, anthraquinones and triarylmethane dyes discharged from printing and dyeing factories also have certain carcinogenic effects [1]. Moreover, the excessive discharge into water stream of antibiotics represented by recalcitrant ciprofloxacin (CIP) possesses a serious threat to humans and the aquatic environment [2]. Therefore, it is very necessary to dispose industrial wastewater effectively.

Organic matter in industrial wastewater has stable physical and chemical properties, and is difficult to be degraded in nature. Among treatment technologies over industrial wastewater, photocatalysis has been paid more attention, due to its mild reaction condition, no secondary treatment, ability to degrade refractory matters and more thorough treatment [3].

Photocatalytic materials are the core part of photocatalytic technology. Currently, TiO$_2$, ZnO and other photocatalysts are widely used [4, 5]. However, these metal-containing photocatalysts are difficult to recover, and will cause harm to the ecosystem if they enter water.

Graphitic carbon nitride (g-C$_3$N$_4$) is a metal-free photocatalytic material with visible light response [6]. It is widely researched, because it is insoluble in water, sensitive to visible light, chemically stable, non-toxic and metal-free [7]. However, g-C$_3$N$_4$ has some disadvantages, such as small specific surface area, few active sites, narrow light absorption range and high photogenic carrier recombination rate, which hinder its wider application [8]. A large number of studies have shown that the shortcomings of g-C$_3$N$_4$ can be effectively solved and the photocatalytic performance can be improved, through modification methods such as element doping [9], defect engineering [10], morphology control [11] and construction of heterogeneous structure [12]. However, the improvement still does not achieve satisfactory results.

In this paper, alkaline activation of g-C$_3$N$_4$ was carried out to improve the specific surface area, increase the active sites, widen the optical response range and improve the photogenic carrier separation, so as to improve the photocatalytic activity of g-C$_3$N$_4$ under visible light.

2. EXPERIMENTAL

2.1. Materials

Urea and sodium hydroxide were purchased from Xilong Chemical Reagent Co., LTD., and Methyl Orange (MO), Rhodamine B (RhB) and ciprofloxacin (CIP) were purchased from China Sinopharm Group. All of them were of analytical purity.

The 50 g urea was sealed and wrapped with tin foil into a crucible, heating to 550 °C for 2 h at 0.5 °C/min. After naturally reducing to room temperature, about 1 g of yellow g-C$_3$N$_4$ powder was obtained. The pure g-C$_3$N$_4$ powder was soaked in 10 mL 0.1 mol/L NaOH solution for 24 h, then centrifuged, filtered and dried to obtain alkaline activated g-C$_3$N$_4$ powder, which was recorded as NaOH-g-C$_3$N$_4$.

∗ Corresponding author. Tel.: +86-791-88136768.
E-mail address: *37143565@qq.com* (SL. Feng)

2.2. Characterization

The crystal structures were analysed by an X-ray powder diffractometer (XRD, Bruker D8, German), with Cu Kα radiation ($\lambda = 0.15418$ nm) with a scanning angle of $5 - 80°$ and a scanning rate of $2 - 4$ °/min. The micromorphology was observed by scanning electron microscope (SEM, Quanta 250FEG, USA FEI Co., Ltd.) with a voltage of 20 kV and a current of 20 mA, and by a high-resolution transmission electron microscope (TEM, Tecnai G220, USA FEI Co., Ltd.) operated at 200 kV. Nitrogen adsorption and desorption test was performed at 77 K with ASAP2460 made by Micromeritics. Before the test, the powder was dried for 12 h at 60 °C. The specific surface area (S.S.A) and pore volume/ pore size were calculated by Brunauer-Emmett-Teller (BET) and Barrett-Joyner-Halenda (BJH) methods, respectively. X-ray photoelectron spectroscopy (XPS) was employed through an ESCALAB 250XI (Thermo Scientific, USA) to study the surface chemical states. The UV-Vis diffuse reflectance spectra (UV-Vis DRS) were determined by a photometer (Lambda950, USA PerkinElmer Corporation) with $BaSO_4$ as the reference sample. Fluorescence analysis (PL) was performed using a fluorescence analyser (F4600, Japan Hitachi).

2.3. Photocatalytic measurement

The photocatalytic degradation experiment was done at about 20 cm under a 3 W blue LED lamp (wavelength: $450 - 480$ nm), with RhB and MO as the target degradants. A photocatalyst of 0.05 g was added to a 50 mL 10 mg/L dye solution, dispersed by ultrasonic for 5 min, and stirred for 30 min in dark place to achieve adsorption equilibrium. After irradiation, about 3 mL solution was extracted every 60 min, centrifuged at 14000 r/min for 1 min. And then the light transmittance was tested on a visible spectrophotometer (721, China Shanghai Lab Spectrum Instruments Co., Ltd.), with the maximum absorption wavelength of RhB and MO at 554 and 460 nm, respectively. The change of dye solution concentration, C/C_0, were calculated, according to a concentration – light transmittance standard curve. C was the concentration after some degradation time, and C_0 was the initial concentration of dye solution. The degradation efficiency is characterized by the following formula:

$$\text{degradation efficiency } \% = (1 - C/C_0) \times 100 \%. \qquad (1)$$

CIP were used to evaluate the antibiotics degradation performance of photocatalysts. The photocatalysts of 0.1 g was added into 100 mL of 10 mg/L CIP solution. The test condition and procedure were the same to that of dyes degradation. The concentration change was analysed using a UV-Vis spectrophotometer (752, China Shanghai Jinghua Instruments Co., Ltd.) at an absorption wavelength of 276 nm.

3. RESULTS AND DISCUSSION

3.1. Phase composition

Fig. 1 shows the XRD patterns of g-C_3N_4 before and after alkaline activation. Before activation, g-C_3N_4 had a peak on 13.1° and 27.6°, respectively. The wide peak corresponding to 13.1° was a plane diffraction peak formed by the periodic arrangement of N and C atoms on the g-C_3N_4 (100) crystal plane, while the sharp diffraction peak at 27.6° corresponded to the periodic arrangement of g-C_3N_4 (002) crystal plane [13]. After the activation of g-C_3N_4 by NaOH, no new heteropeaks appeared in the XRD patterns, indicating that impurities were not introduced into g-C_3N_4 during the activation process. However, the intensities of the diffraction peaks decreased, indicating that the activation of NaOH destroyed the periodic lattice arrangement of g-C_3N_4, the stacked interlayer structure was loosened, and some nanocrystals were stripped. As can be seen from Fig. 1b, the (002) diffraction peak of g-C_3N_4 shifted to a small angle after NaOH activation, indicating that Na^+ entered the interlayers of g-C_3N_4 and expanded the spacing between layers.

3.2. Microstructure

Fig. 2 depicts the SEM and TEM images of g-C_3N_4 before and after alkaline activation. As can be seen from Fig. 2 a, g-C_3N_4 without activation was thin flakes and curled at the edges. As shown in Fig. 2b, g-C_3N_4 after alkaline activation was still flake-like. However, there were many pores in the sheets, which caused periodic lattice arrangement failure of g-C_3N_4 and decreased the intensity of XRD diffraction peak, consistent with the analysis results of XRD patterns.
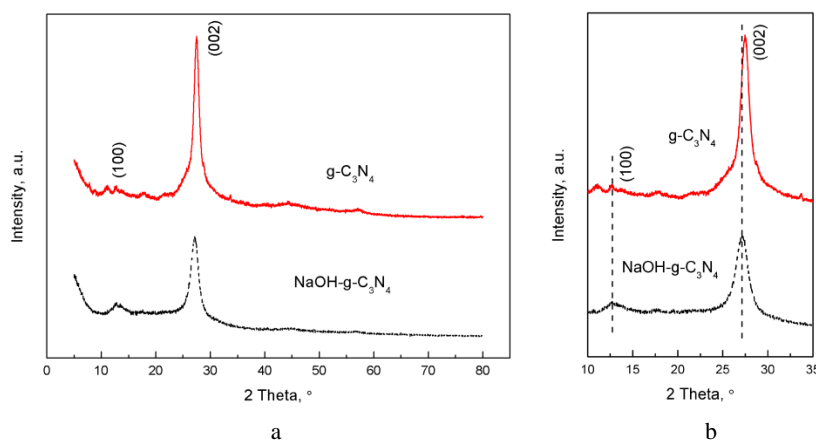

Fig. 1. a – XRD patterns of g-C_3N_4 before and after alkaline activation; b – partial enlarged patterns

The TEM pictures in Fig. 2 c showed that the g-C$_3$N$_4$ powder before activation was large, transparent in the middles and dark at the edges, indicating that the g-C$_3$N$_4$ powder was thin flakes with thick edges. In contrast, Fig. 2 d showed that g-C$_3$N$_4$ powder after alkaline activation had a smaller particle size and plenty of pores in the middles. The powder was more transparent in the middle, and the black edge areas were reduced, indicating that alkaline activation made g-C$_3$N$_4$ powder thinner and reduced the curled edges.

3.3. N$_2$ adsorption desorption test

Fig. 3 illustrates the N$_2$ adsorption-desorption curve of g-C$_3$N$_4$ before and after alkaline activation. The powder before and after g-C$_3$N$_4$ activation had a type IV adsorption-desorption isotherms containing a H3 hysteresis loop [14], indicating that the pore size of the powder was located in the mesoporous range and the pore shape was thin plate. After alkaline activation, the pores in g-C$_3$N$_4$ powder increased significantly, which was the same as the results of TEM. The specific surface areas of g-C$_3$N$_4$ before and after alkaline activation were 36.05 and 68.81 cm^2 g^{-1}, respectively, the pore volumes were 0.18 and 0.53 cm^3 g^{-1}, respectively, and the average pore diameters were 19.05 and 27.88 nm, respectively. The increase of specific surface area and pore volume was beneficial to the adsorption of pollutant molecules and provided more active sites for photocatalytic degradation.
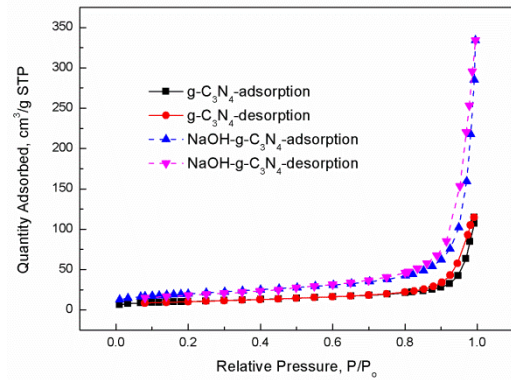

Fig. 3. N$_2$ adsorption- desorption isotherms of g-C$_3$N$_4$ before and after alkaline activation

Table 1. Pore structure parameters of g-C$_3$N$_4$ before and after alkaline activation

Sample	g-C$_3$N$_4$	NaOH-g-C$_3$N$_4$
BET S.S.A, cm^2 g^{-1}	36.05	68.81
BJH pore volume, cm^3 g^{-1}	0.18	0.53
BJH average pore size, nm	19.05	27.88

3.4. Surface chemical states

Fig. 4 shows the XPS spectra of g-C$_3$N$_4$ activation before and after alkaline activation. Before activation, g-C$_3$N$_4$ powder surface contained three elements of C, N and O in the survey spectra of Fig. 4 a. O elements came from residual oxygen after the precursor urea thermal polymerization [15].
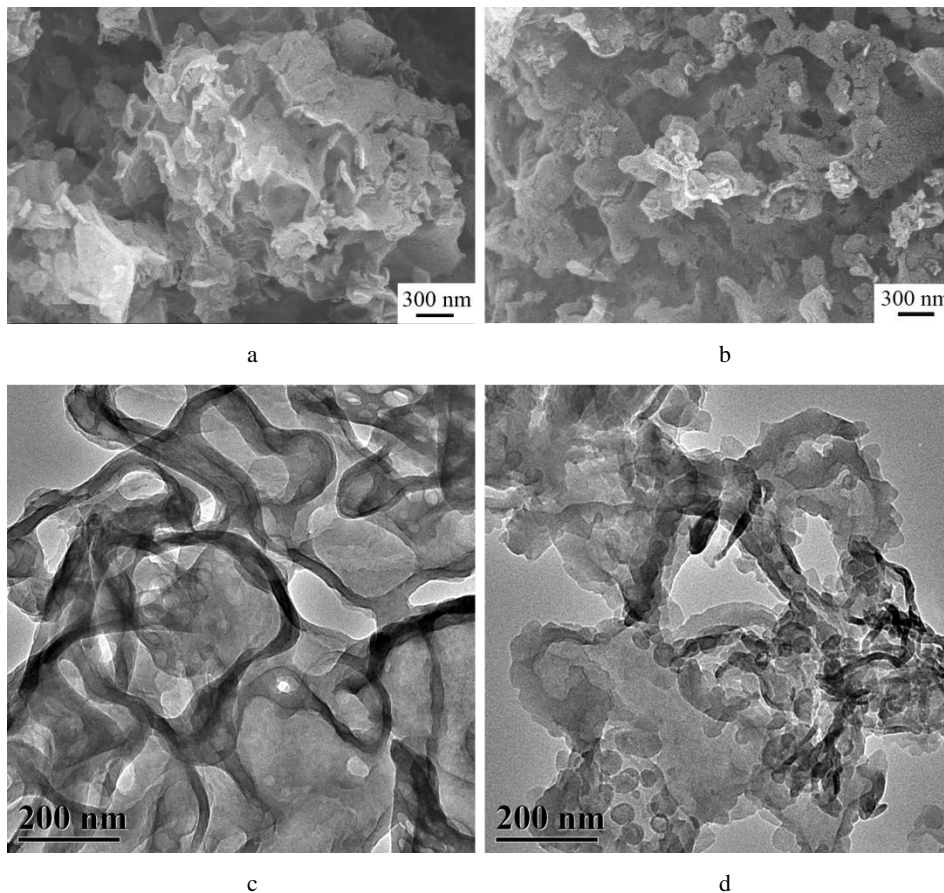

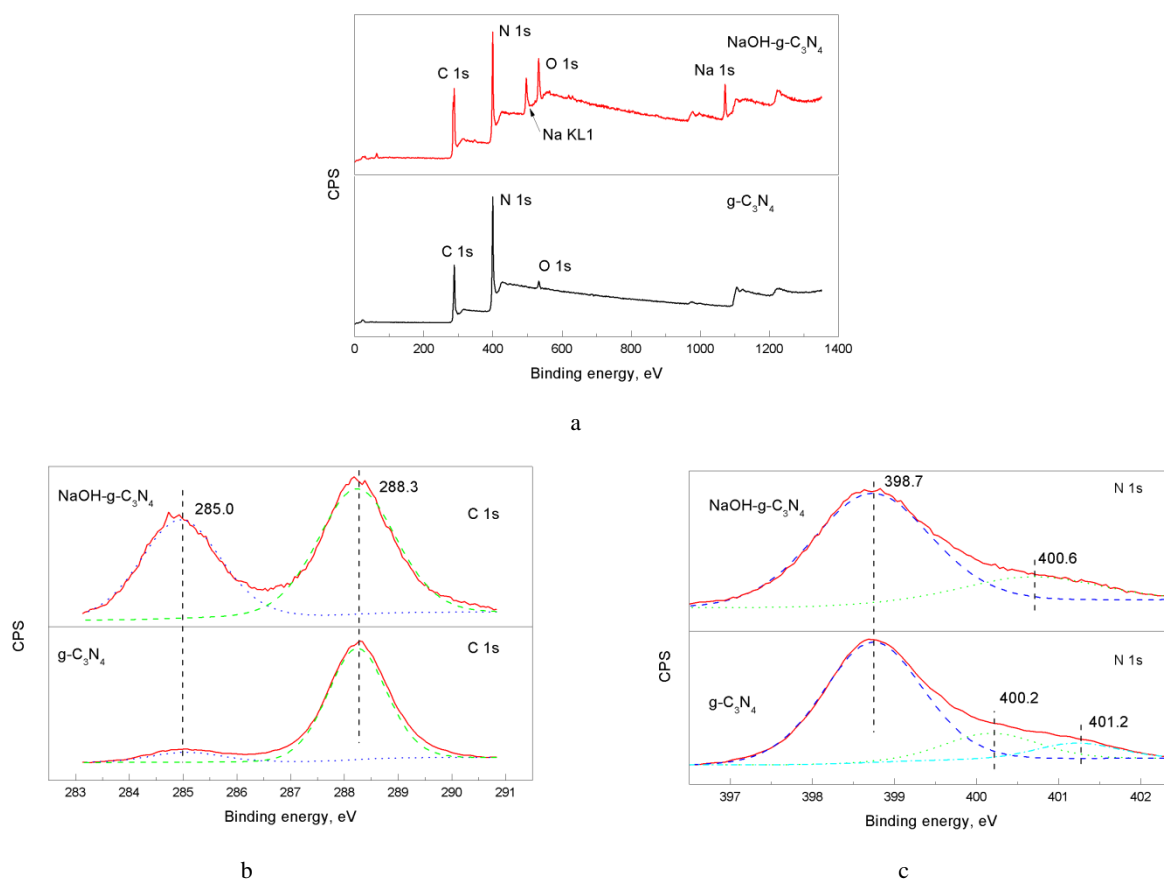**Fig. 2.** a, b – SEM images; c, d – TEM pictures of g-C$_3$N$_4$ before (a, c) and after (b, d) alkaline activation

a

b

c

Fig. 4. XPS spectra of g-C_3N_4 before and after alkaline activation: a – survey; b – C 1 s; c – N 1 s

After activation, g-C_3N_4 showed four elements of C, N, O and Na. The content of O element was significantly higher than that of the g-C_3N_4 before activation, due to the O element from residual oxygen after urea polymerization and NaOH. Fig. 4 b is the high-resolution XPS spectra of C 1s, where the peaks of 285.0 and 288.3 eV corresponded to the graphite carbon atom (C-C) and aromatic sp^2 hybrid carbon (N-C=N) in g-C_3N_4, respectively [16]. Fig. 4 c shows that different types of N in g-C_3N_4: C-N=C (398.73 eV), N-$(C)_3$ (400.18 eV) and N-H (401.23 eV) [17]. After alkaline activation of g-C_3N_4, N-H bonds disappeared, demonstrating that the H in N-H and OH^- in NaOH combined into H_2O. The N-$(C)_3$ binding energy increased, because the lone pair electrons of N in N-$(C)_3$ formed the coordination bonds with Na^+, the density of electron clouds around the N atoms was reduced, and the extranuclear bounding ability of N nucleus raised.

3.5. Optical properties

The UV-Vis DRS curves of g-C_3N_4 powder before and after alkaline activation are shown in Fig. 5 a. The absorption edge of g-C_3N_4 before alkaline activation was about 465 nm.
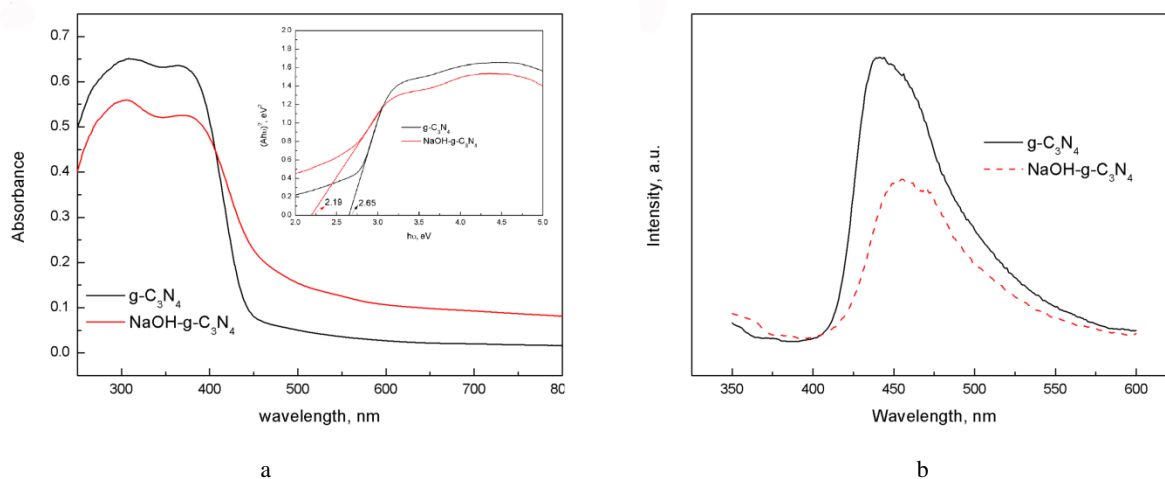

a

b

Fig. 5. g-C_3N_4 before and after alkaline activation: a – UV-Vis DRS; b – PL spectra

132

After alkaline activation, the absorption edge of g-C$_3$N$_4$ was redshifted and reached about 560 nm, which could be attributed to the effect of Na$^+$ [18]. The badganp width can be calculated according to Kubelka-Munk formula [19]:

$$\alpha h\upsilon = A(h\upsilon - E_g)^{n/2}, \qquad (2)$$

where α is the absorption coefficient; h is the planck constant; υ is the frequency of light; A is a constant; E_g is the bandgap width. For indirect gap semiconductors such as g-C$_3$N$_4$; n equalled to 1 [20]. As shown in Fig. 5 b, the band gap widths of g-C$_3$N$_4$ before and after alkaline activation were 2.65 and 2.19 eV, respectively. The reduction of the band gap width was beneficial to broaden the light response range and absorb more light for photocatalytic reaction.

Fig. 5 b depicts the PL spectra of g-C$_3$N$_4$ before and after alkaline activation. After alkaline activation, the luminous frequency of g-C$_3$N$_4$ was redshifted, which was consistent with the analysis results in UV-Vis DRS. The higher the intensity of PL spectrum, the higher the probability of photoelectron and hole recombination [21]. The PL intensity of g-C$_3$N$_4$ was significantly quenched after alkaline activation, indicating that photogenic carriers were effectively separated, which was helpful to enhance photocatalytic efficiency.

3.6. Photocatalytic performances

Fig. 6 a shows the degradation curves of RhB and MO by g-C$_3$N$_4$ powder. It can be seen that RhB and MO hardly degraded under the irradiation of 3W blue LED lamp with a wavelength of 450 – 480 nm. After 30 min stirring to reach adsorption equilibrium, the C/C$_0$ values of MO and RhB

solutions adsorbed by g-C$_3$N$_4$ with activation were 0.87 and 0.47, respectively. The C/C$_0$ values of MO and RhB solutions adsorbed by g-C$_3$N$_4$ after alkaline activation were 0.80 and 0.19, respectively. The adsorption of RhB by g-C$_3$N$_4$ was better than that of MO. This might be because the cationic dye RhB was positively charged in aqueous solution, the anionic dye MO was negatively charged [22]. And the Zeta potential of g-C$_3$N$_4$ was about 30.3 mV (pH = 7) [23], g-C$_3$N$_4$ was also negatively charged in neutral solution. Under electrostatic action, g-C$_3$N$_4$ powder tended to adsorb RhB molecules and repelled MO molecules. For the same dye (RhB or MO), the specific surface area and pore volume of alkaline activated g-C$_3$N$_4$ were greater than g-C$_3$N$_4$ without activation, so the adsorption capacity of alkaline activated g-C$_3$N$_4$ over dye molecules was also greater that g-C$_3$N$_4$ without activation. After photocatalytic degradation for 300 min, the C/C$_0$ values of MO and RhB degraded by g-C$_3$N$_4$ without activation were 0.78 and 0.04, respectively. And the C/C$_0$ values of MO and RhB degraded by alkaline activated g-C$_3$N$_4$ were 0.55 and 0.007, respectively. There were many factors affecting the photocatalysis of dyes, including the structure of dyes, dye concentration and volume, solution pH, frequency and intensity of light source. g-C$_3$N$_4$ powder degraded RhB faster than MO, demonstrating that the molecular structure of dyes was also important, in addition to the electrostatic interaction. Alkaline activated g-C$_3$N$_4$ degraded RhB and MO at a faster rate than non-activated g-C$_3$N$_4$, demonstrating that alkaline activated g-C$_3$N$_4$ could absorb more light, had lower photogenic carrier recombination, larger specific surface area and more active sites.
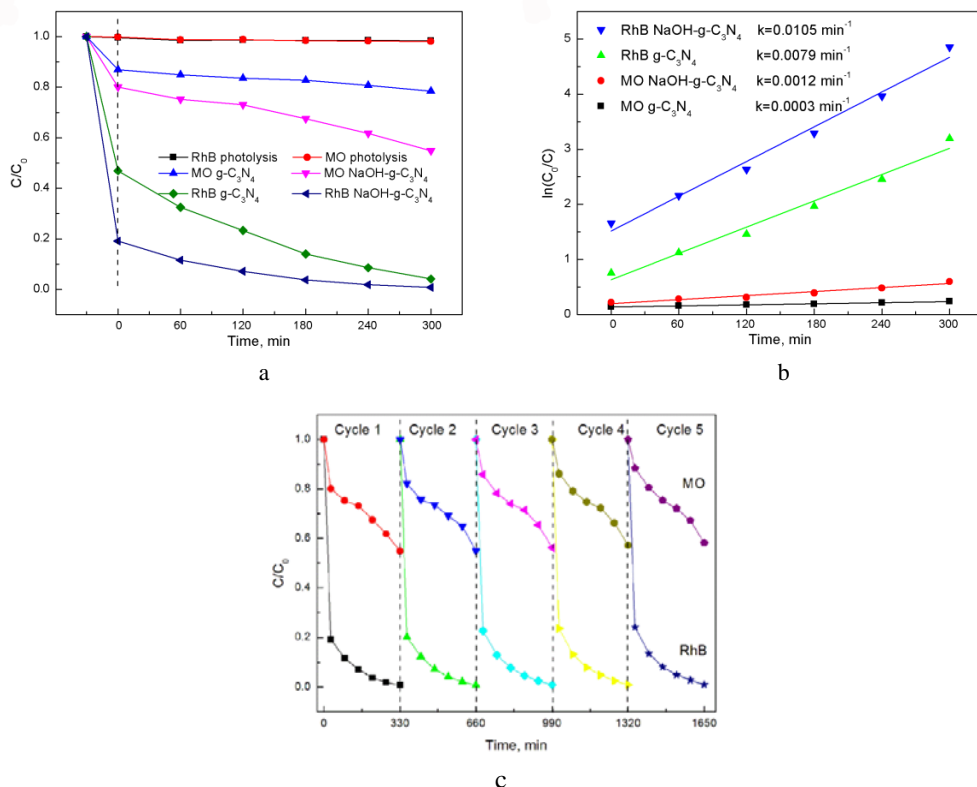

a

b

c

Fig. 6. g-C$_3$N$_4$ before and after alkaline activation: a – photocatalytic degradation curves; b – degradation kinetic curves; c – reusability performance

The kinetic curves of photocatalytic degradation of dyes by g-C$_3$N$_4$ are shown in Fig. 6 b. The degradation curves were in line with the pseudo-first-order kinetics. The degradation rate constants of RhB and MO by unactivated g-C$_3$N$_4$ were 0.0079 and 0.0003 min^{-1}, respectively. The degradation rate constants of RhB and MO by alkaline activated g-C$_3$N$_4$ were 0.0105 and 0.0012 min^{-1}, respectively. The degradation rate constants of dyes by alkaline activated g-C$_3$N$_4$ were significantly higher than that of inactivated g-C$_3$N$_4$, furtherly indicating the superior photocatalytic activity of alkaline activated g-C$_3$N$_4$.

The results of some recent works on the application of g-C$_3$N$_4$ photocatalyst in dyes degradation are shown in Table 2. It can be seen that the NaOH treated g-C$_3$N$_4$ showed a competitive degradation efficiency under just than 3W LED light. To evaluate the stability of NaOH-g-C$_3$N$_4$ photocatalyst, recycling experiments to degrade RhB and MO was conducted, and the results are illustrated in Fig. 6 c. After consecutive 5 cycles with every round including adsorption equilibrium of 30 min and photocatalysis of 300 min, the degradation efficiencies of MO and RhB were 41.8 % and 99.0 %, which were just slighter lower than those of the first round, indicating the superior stability and reusability of alkaline treated g-C$_3$N$_4$.

In addition to dye pollutants, antibiotics are also a class of refractory pollutants. Due to its carcinogenicity and low biodegradability in wastewater, CIP was chosen to evaluate photocatalytic performance of alkaline activated g-C$_3$N$_4$ photocatalyst. Fig. 7 a depicts the photocatalytic degradation performance of the photocatalysts under LED light irradiation. Without photocatalysts, the photolysis of CIP was negligible, revealing that CIP was a persistent organic pollutant. After 30 min dark adsorption, the C/C$_0$ values of g-C$_3$N$_4$ and NaOH-g-C$_3$N$_4$ were 0.89 and 0.81, respectively, which demonstrated NaOH-g-C$_3$N$_4$ had higher S.S.A than g-C$_3$N$_4$. After 300 min irradiation under LED light, the C/C$_0$ values of g-C$_3$N$_4$ and NaOH-g-C$_3$N$_4$ reached 0.70 and 0.61, respectively. The higher CIP photocatalytic efficiency furtherly indicated the superior photocatalytic performance of NaOH-g-C$_3$N$_4$. Fig. 7 b illustrates the reusability of NaOH-g-C$_3$N$_4$ towards CIP degradation. In the 5 runs, the degradation efficiencies of NaOH-g-C$_3$N$_4$ reduced slightly, demonstrating the good reusability of alkaline activated g-C$_3$N$_4$. Table 3 shows some recent works on the CIP degradation of g-C$_3$N$_4$ based photocatalyst. It can be indicated that the alkaline activated g-C$_3$N$_4$ had a good degradation property under low-power LED light.

4. CONCLUSIONS

Pure g-C$_3$N$_4$ photocatalyst was prepared by sealed pyrolysis of urea, and alkaline activated g-C$_3$N$_4$ powder was prepared by NaOH immersion method. The results showed that Na$^+$ entered the layers of alkaline activated g-C$_3$N$_4$, expanded the spacing between layers.

Table 2. The comparison of g-C$_3$N$_4$ base photocatalyts for the degradation of dyes

Dye			Photocatalyst		Irradiation condition	Degradation efficiency and time	Photocatalytic rate constant	Reference
Category	Volume	C$_0$	Category	Weight				
Orange II	40 mL	10 mg/L	g-C$_3$N$_4$	20 mg	300 W, λ > 420 nm, intensity: 15 mW cm^{-2}	50 % (180 min)	0.00411 min^{-1}	[25]
RhB	100 mL	20 mg/L	g-C$_3$N$_4$	10 mg	300 W, λ > 420 nm, intensity: ca. 100 mW cm^{-2}	4.8 % (30 min)	–	[26]
Malachite 91 green (MG)	50 mL	20 mg/L	g-C$_3$N$_4$	20 mg	350 W, λ > 420 nm	40 % (90 min)	0.0057 min^{-1}	[27]
Amino Black 10B (AB 10B)						34.7 % (90 min)	0.0049 min^{-1}	
RhB	50 mL	10 mg/L	g-C$_3$N$_4$/ZrO$_2$	30 mg	300 W, 420 nm < λ < 760 nm	82 % (150 min)	–	[28]
Methyl orange (MO)						50 % (150 min)		
Acid orange II (AO II)						98 % (150 min)		
RhB	100 mL	10 mg/L	g-C$_3$N$_4$	10 mg	2 × 200 W, 5 cm from dye solution	35 % (120 min)	0.0029 min^{-1}	[29]
MO						10 % (120 min)	0.0008 min^{-1}	
Methylene blue (MB)	10 mL	10 mg/L	g-C$_3$N$_4$	20 mg	18 W LED light, 14 mW/cm^2	61 % (60 min)	0.016 min^{-1}	[30]
Methylene blue (MB)	100 mL	10 ppm	g-C$_3$N$_4$	50 mg	20 W domestic LED white light, 20 mW cm^{-2}, 10 cm from solution surface	49 % (60 min)	0.0111 min^{-1}	[31]
MO	50 mL	10 mg/L	NaOH-g-C$_3$N$_4$	0.05 g	3 W blue LED lamp, 20 cm over dyes surface, λ: 450 – 480 nm	45 % (300 min)	0.0012 min^{-1}	in this study
RhB						99.3 % (300 min)	0.0105 min^{-1}	

<center>a</center>
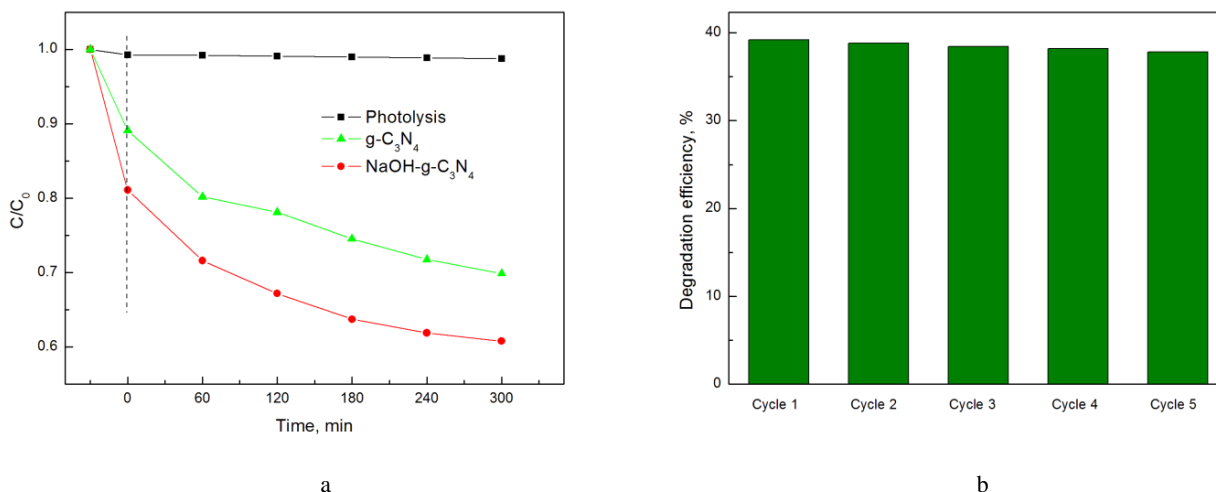
<center>b</center>

Fig. 7. a – CIP photocatalytic degradation curves; b – reusability perfomance

Table 3. The comparison of g-C$_3$N$_4$ base photocatalyts for the degradation of CIP

CIP volume	CIP C$_0$	Catalyst category	Catalyst weight	Irradiation condition	Degradation efficiency and time	Reference
50 mL	20 mg/L	g-C$_3$N$_4$	20 mg	300 W Xenon lamp, λ > 420 nm	ca.56 % (60 min)	32
100 mL	10 ppm	g-C$_3$N$_4$	0.1 g	500 W halogen lamp	50.2 % (2 h)	33
50 mL	15 µmol L^{-1}	g-C$_3$N$_4$	10 mg	500 W Xenon lamp	30 % (120 min)	34
50 mL	10 mg/L	g-C$_3$N$_4$	20 mg	500 W Xenon lamp, λ > 380 nm	13 % (60 min)	35
50 mL	20 ppm	S-g-C$_3$N$_4$	75 mg	15 W UV-A (λ: 320 – 400 nm)	60 % (210 min)	36
100 mL	10 mg/L	NaOH-g-C$_3$N$_4$	10 mg	3 W LED light	39 % (300 min)	in this study

The specific surface area and pore volume of the powder were increased, the coordination bonds by N-(C)$_3$ lone pair electrons and Na$^+$ was formed, the bandgap width was decreased, and the photogenic carrier recombination were reduced.

Alkaline activated g-C$_3$N$_4$ has better adsorption and degradation performance over RhB and MO than inactivated g-C$_3$N$_4$. Our results pave the way for effective g-C$_3$N$_4$ modification through a simple alkaline treatment method towards efficient solar energy utilization and organic wastewater degradation.

REFERENCES

1. **Vakili, M., Rafatullah, M., Salamatinia, B., Abdullah, A.Z., Ibrahim, M.H., Tan, K.B., Gholami, Z., Amouzgar, P.** Application of Chitosan and Its Derivatives as Adsorbents for Dye Removal from Water and Wastewater: A Review *Carbohydrate Polymers* 113 2014: pp. 115 – 130. https://doi.org/10.1016/j.carbpol.2014.07.007

2. **Lai, C., Zhang, M., Li, B., Huang, D., Zeng, G., Qin, L., Liu, X., Yi, H., Cheng, M., Li, L., Chen, Z., Chen, L.** Fabrication of CuS/BiVO$_4$ (040) Binary Heterojunction Photocatalysts with Enhanced Photocatalytic Activity for Ciprofloxacin Degradation and Mechanism Insight *Chemical Engineering Journal* 358 2019: pp. 891 – 902. https://doi.org/10.1016/j.cej.2018.10.072

3. **Wei, Q., Yang, D., Fan, M., Harris, H.G.** Applications of Nanomaterial-based Membranes in Pollution Control *Critical Reviews in Environmental Science and Technology* 43 (22) 2013: pp. 2389 – 2438. https://doi.org/10.1080/10643389.2012.672066

4. **Zhang, W., Li, Y., Su, Y., Mao, K., Wang, Q.** Effect of Water Composition on TiO$_2$ Photocatalytic Removal of Endocrine Disrupting Compounds (EDCs) and Estrogenic Activity from Secondary Effluent *Journal of Hazardous Materials* 215 – 216 2012: pp. 252 – 258. https://doi.org/10.1016/j.jhazmat.2012.02.060

5. **Feng, S., Song, J., Liu, F., Fu, X., Guo, H., Zhu, J., Zeng, Q., Peng, X., Wang, X., Ouyang, Y., Li, F.** Photocatalytic Properties, Mechanical Strength and Durability of TiO$_2$ Cement Composites Prepared by A Spraying Method for Removal of Organic Pollutants *Chemosphere* 254 2020: pp. 126813. https://doi.org/10.1016/j.chemosphere.2020.126813

6. **Noman, M.T., Petru, M., Militký, J., Azeem, M., Ashraf, M.A.** One-pot Sonochemical Synthesis of ZnO Nanoparticles for Photocatalytic Applications, Modelling and Optimization *Materials* 13 2020: pp. 14. https://doi.org/10.3390/ma13010014

7. **Wang, X., Maeda, K., Thomas, A., Takanabe, K., Xin, G., Carlsson, J.M., Domen, K., Antonietti, M.** A Metal-free Polymeric Photocatalyst for Hydrogen Production from Water under Visible Light *Nature Materials* 8 (1) 2009: pp. 76–80.
https://doi.org/10.1142/9789814317665_0039

8. **Talapaneni, S.N., Singh, G., Kim, I.Y., AlBahily, K., Al-Muhtaseb, A.H., Karakoti, A.S., Tavakkoli, E., Vinu, A.** Nanostructured Carbon Nitrides for CO_2 Capture and Conversion *Advanced Materials* 32 (18) 2019: pp. 1904635.
https://doi.org/10.1002/adma.201904635

9. **Kessler, F.K., Zheng, Y., Schwarz, D., Merschjann, C., Schnick, W., Wang, X., Bojdys, M.J.** Functional Carbon Nitride Materials-design Strategies for Electrochemical Devices *Nature Reviews Materials* 2 2017: pp. 17030.
https://doi.org/10.1038/natrevmats.2017.30

10. **Yu, Y., Yan, W., Wang, X., Li, P., Gao, W., Zou, H., Wu, S., Ding, K.** Surface Engineering for Extremely Enhanced Charge Separation and Photocatalytic Hydrogen Evolution on g-C_3N_4 *Advanced Materials* 30 (9) 2018: pp. 1705060.
https://doi.org/10.1002/adma.201705060

11. **Yang, P., Wang, R., Zhou, M., Wang, X.** Photochemical Construction of Carbonitride Superstructures for Red-light Redox Catalysis *Angewandte Chemie International Edition* 57 2018: pp. 8674.
https://doi.org/10.1002/anie.201804996

12. **Wang, Y., Du, P., Pan, H., Fu, L., Zhang, Y., Chen, J., Du, Y., Tang, N., Liu, G.** Increasing Solar Absorption of Atomically Thin 2D Carbon Nitride Sheets for Enhanced Visible-light Photocatalysis *Advanced Materials* 31 (40) 2019: pp. 1807540.
https://doi.org/10.1002/adma.201807540

13. **Zheng, Y., Lin, L.H., Wang, B., Wang, X.C.** Graphitic Carbon Nitride Polymers toward Sustainable Photoredox Catalysis *Angewandte Chemie International Edition* 54 (44) 2015: pp. 12868.
https://doi.org/10.1002/anie.201501788

14. **Gao, J., Zhou, Y., Li, Z., Yan, S., Wang, N., Zou, Z.** High-yield Synthesis of Millimetre-long, Semiconducting Carbon Nitride Nanotubes with Intense Photoluminescence Emission and Reproducible Photoconductivity *Nanoscale* 4 (12) 2012: pp. 3687.
https://doi.org/10.1039/c2nr30777d

15. **Shang, Y., Chen, X., Liu, W., Tan, P., Chen, H., Wu, L., Ma, C., Xiong, X., Pan, J.** Photocorrosion Inhibition and High-efficiency Photoactivity of Porous g-C_3N_4/Ag_2CrO_4 Composites by Simple Microemulsion-assisted Co-precipitation Method *Applied Catalysis B- Environmental* 204 2017: pp. 78–88.
https://doi.org/10.1016/j.apcatb.2016.11.025

16. **Sun, Z., Fischer, J.M.T.A., Li, Q., Hu, J., Tang, Q., Wang, H., Wu, Z., Hankel, M., Searles, D.J., Wang, L.** Enhanced CO_2 Photocatalytic Reduction on Alkali-decorated Graphitic Carbon Nitride *Applied Catalysis B- Environmental* 216 2017: pp. 146–155.
https://doi.org/10.1016/j.apcatb.2017.05.064

17. **Xiao, N., Li, S., Liu, S., Xu, B., Li, Y., Gao, Y., Ge, L., Lu, G.** Novel PtPd Aalloy Nanoparticle-decorated g-C_3N_4 Nanosheets with Enhanced Photocatalytic Activity for H_2 Evolution under Visible Light Irradiation *Chinese Journal of Catalysis* 40 (3) 2019: pp. 352–361.
https://doi.org/10.1016/S1872-2067(18)63180-8

18. **Thaweesak, S., Lyu, M., Peerakiatkhajohn, P., Butburee, T., Luo, B., Chen, H., Wang, L.** Two-Dimensional g-C_3N_4/$Ca_2Nb_2TaO_{10}$ Nanosheet Composites for Efficient Visible Light Photocatalytic Hydrogen Evolution *Applied Catalysis B- Environmental* 202 2017: pp. 184–190.
https://doi.org/10.1016/j.apcatb.2016.09.022

19. **Shang, Y., Ma, Y., Chen, X., Xiong, X., Pan, J.** Effect of Sodium Doping on the Structure and Enhanced Photocatalytic Hydrogen Evolution Performance of Graphitic Carbon Nitride *Molecular Catalysis* 433 2017: pp. 128–135.
https://doi.org/10.1016/j.mcat.2016.12.021

20. **Han, X., Dong, S., Yu, C., Wang, Y., Yang, K., Sun, J.** Controllable Synthesis of Sn-doped BiOCl for Efficient Photocatalytic Degradation of Mixed-dye Wastewater under Natural Sunlight Irradiation *Journal of Alloys and Compouds* 685 2016: pp. 997–1007.
https://doi.org/10.1016/j.jallcom.2016.06.298

21. **Meng, S., Ning, X., Zhang, T., Chen, S.F., Fu, X.** What is the Transfer Mechanism of Photogenerated Carriers for the Nanocomposite Photocatalyst Ag_3PO_4/g-C_3N_4, Band-band Transfer or a Direct Z-scheme? *Physical Chemistry Chemical Physics* 17 2015: pp. 11577–11585.
https://doi.org/10.1039/C5CP01523E

22. **Shi, Z., Zhang, Y., Shen, X., Duoerkun, G., Zhu, B., Zhang, L., Li, M., Chen, Z.** Fabrication of g-C_3N_4/BiOBr Heterojunctions on Carbon Fibers as Weaveable Photocatalyst for Degrading Tetracycline Hydrochloride under Visible Light *Chemical Engineering Journal* 386 2020: pp. 124010.
https://doi.org/10.1016/j.cej.2020.124010

23. **Yang, X., Qian, F., Zou, G., Li, M., Lu, J., Li, Y., Bao, M.** Facile Fabrication of Acidified g-C_3N_4/g-C_3N_4 Hybrids with Enhanced Photocatalysis Performance under Visible Light Irradiation *Applied Catalysis B- Environmental* 193 2016: pp. 22–35.
https://doi.org/10.1016/j.apcatb.2016.03.060

24. **Sun, X., Jiang, D., Zhang, L., Wang, W.** Alkaline Modified g-C_3N_4 Photocatalyst for High Selective Oxide Coupling of Benzyl Alcohol to Benzoin *Applied Catalysis B- Environmental* 220 2018: pp. 553–560.
https://doi.org/10.1016/j.apcatb.2017.08.057

25. **Tatykayev, B., Chouchene, B., Balan, L., Gries, T., Medjahdi, G., Girot, E., Uralbekov, B., Schneider, R.** Heterostructured g-CN/TiO_2 Photocatalysts Prepared by Thermolysis of g-CN/MIL-125(Ti) Composites for Efficient Pollutant Pegradation and Hydrogen Production *Nanomaterials* 10 2020: pp. 1387.
https://doi.org/10.3390/nano10071387

26. **Liang, Q., Liu, X., Wang, J., Liu, Y., Liu, Z., Tang, L., Shao, B., Zhang, W., Gong, S., Cheng, M., He, Q., Feng, C.** In-situ Self-assembly Construction of Hollow Tubular g-C_3N_4 Isotype Heterojunction for Enhanced Visible-light Photocatalysis: Experiments and Theories *Journal of Hazardous Materials* 41 2021: pp. 123355.
https://doi.org/10.1016/j.jhazmat.2020.123355

27. **Xu, X., Wang, S., Hu, T., Yu, X., Wang, J., Jia, C.** Fabrication of Mn/O Co-doped g-C_3N_4: Excellent Charge Separation and Transfer for Enhancing Photocatalytic Activity under Visible Light Irradiation *Dyes and Pigments* 175 2020: pp. 108107.
https://doi.org/10.1016/j.dyepig.2019.108107

28. **Zhang, K., Zhou, M., Yu, C., Yang, K., Li, X., Dai, W., Guan, J., Shu, Q., Huang, W.** Construction of S-scheme g-C_3N_4/ZrO_2 Heterostructures for Enhancing Photocatalytic Disposals of Pollutants and Electrocatalytic Hydrogen Evolution *Dyes and Pigments* 180 2020: pp. 108525.
https://doi.org/10.1016/j.dyepig.2020.108525

29. **Paul, D.R., Nehra, S.P.** Graphitic Carbon Nitride: a Sustainable Photocatalyst for Organic Pollutant Degradation and Antibacterial Applications *Environmental Science and Pollution Research* 28 2020: pp. 3888 – 3896.
https://doi.org/10.1007/s11356-020-09432-6

30. **Ghosh, U., Pal, A.** Fabrication of a Novel Bi_2O_3 Nanoparticle Impregnated Nitrogen Vacant 2D g-C_3N_4 Nanosheet Z Scheme Photocatalyst for Improved Degradation of Methylene Blue Dye under LED Light Illumination *Applied Surface Science* 507 2020: pp. 144965.
https://doi.org/10.1016/j.apsusc.2019.144965

31. **Pal, K., Mondal, A., Jana, R., Ray, P.P., Gayen, A.** Domestic LED Light Driven Methylene Blue Degradation by g-C_3N_4-$CaCu_3Ti_4O_{12}$ Composite *Applied Surface Science* 467 – 468 2019: pp. 543 – 553.
https://doi.org/10.1016/j.apsusc.2018.10.176

32. **He, R., Xue, K., Wang, J., Yan, Y., Peng, Y., Yang, T., Hu, Y., Wang, W.** Nitrogen-deficient g-C_3N_x/POMs Porous Nanosheets with P-N Heterojunctions Capable of the Efficient Photocatalytic Degradation of Ciprofloxacin *Chemosphere* 259 2020: pp. 127465.
https://doi.org/10.1016/j.chemosphere.2020.127465

33. **Samsudin, M.F.R., Frebillot, C., Kaddoury, Y., Sufian, S., Ong, W.J.** Bifunctional Z-scheme $Ag/AgVO_3/g$-C_3N_4 Photocatalysts for Expired Ciprofloxacin Degradation and Hydrogen Production from Natural Rainwater without Using Scavengers *Journal of Environmental Management* 270 2020: pp. 110803.
https://doi.org/10.1016/j.jenvman.2020.110803

34. **Hu, K., Li, R., Ye, C., Wang, A., Wei, W., Hu, D., Qiu, R., Yan, K.** Facile Synthesis of Z-scheme Composite of TiO_2 Nanorod/g-C_3N_4 Nanosheet Efficient for Photocatalytic Degradation of Ciprofloxacin *Journal of Cleaner Production* 253 2020: pp. 120055.
https://doi.org/10.1016/j.jclepro.2020.120055

35. **Chuaicham, C., Pawar, R.R., Karthikeyan, S., Ohtani, B., Sasaki, K.** Fabrication and Characterization of Ternary Sepiolite/g-C_3N_4/Pd Composites for Improvement of Photocatalytic Degradation of Ciprofloxacin under Visible Light Irradiation *Journal of Colloid and Interface Science* 577 2020: pp. 397 – 405.
https://doi.org/10.1016/j.jcis.2020.05.064

36. **Gupta, B., Gupta, A.K., Ghosal, P.S., Tiwary, C.S.** Photo-Induced Degradation of Bio-toxic Ciprofloxacin using the Porous 3D Dybrid Architecture of an Atomically Thin Sulfur-doped g-C_3N_4/ZnO Nanosheet *Environmental Research* 183 2020: pp. 109154.
https://doi.org/10.1016/j.envres.2020.109154